Title: Pixelated scintillator array response to relativistic electrons

Author(s): Schultz, Kimberly Ann
Carpenter, Matthew Hollis
Espy, Michelle A.
Moir, David C.
Shurter, Roger P.
Sedillo, Robert

Intended for: Report

Issued: 2019-05-23

Pixelated scintillator array response to relativistic electrons

K.A. Schultz, M.H. Carpenter, M.A. Espy, D.C. Moir, R.P. Shurter, B. Sedillo

1. Introduction

In order to make time resolved measurements of the gamma spectra on DARHT Axis 2 using the Compton Spectrometer (CS), the electron detector in the focal plane must be a scintillator that is optically coupled to a gated or streak camera. There are several issues we would like to address with experiments at Idaho Accelerator Center (IAC) before committing to a full size array (7"x2"), which would cost at least $100k. Two candidates for this application are organic (Bicron 422 or equivalent) or inorganic (LYSO) scintillator. Monte Carlo calculations were performed by Rachel Morneau, P-21, using MCNP to compare the two materials each 1.5mm thick for an energy range of 0.1 to 20MeV. The energy loss per particle in LYSO is much larger (100x) than in the plastic scintillator. We confirmed, by performing experiments with the CS on the Microton, that sensitivity of the LYSO was much larger (10x) than the plastic scintillator. Therefore, we have selected LYSO as the scintillator of choice. However, interest in the response of other organic and plastic scintillators prompted an increase in scope of the project.

The goals of this experiment were as follows. First, we need to understand the optical response of the scintillators to electrons as a function of thickness, energy, and deposited charge. We also need to verify level of saturation in the scintillation process. Second, compare the scintillators' response to an image plate (the current CS detector). Third, we need to quantify the effect of signal bleed through to adjacent pixels.

2. Experimental Setup

The experiments were conducted at the Idaho Accelerator Center's 44 MeV short-pulse electron linear induction accelerator (linac). Since the goal is to characterize the response of various scintillators, we used the single pulse mode with a pulse length of 60 ps. The energy of the beam was varied from 5 to 20 MeV. A broad view of the setup is shown in FIG. 1. After acceleration and a 90° bend, the beam passed through a 1-mil Ti window and though a 3" air gap to the Mylar window of the chamber (FIG. 2a). The range of 20-MeV electrons in graphite is 2.5". Therefore, a 3" thick piece of graphite with a 2-mm diameter hole served as a collimator for the beam with a 7.5° half-acceptance angle (FIG. 2b). We held a rough vacuum (around 10^{-3} Torr) in the chamber after failing to get a good (<1 cm) spot size in air on radiochromic at various locations after beam exit.

FIG. 1 Wide view of the setup. The accelerator exit is on the left; the experimental chamber is in the center.
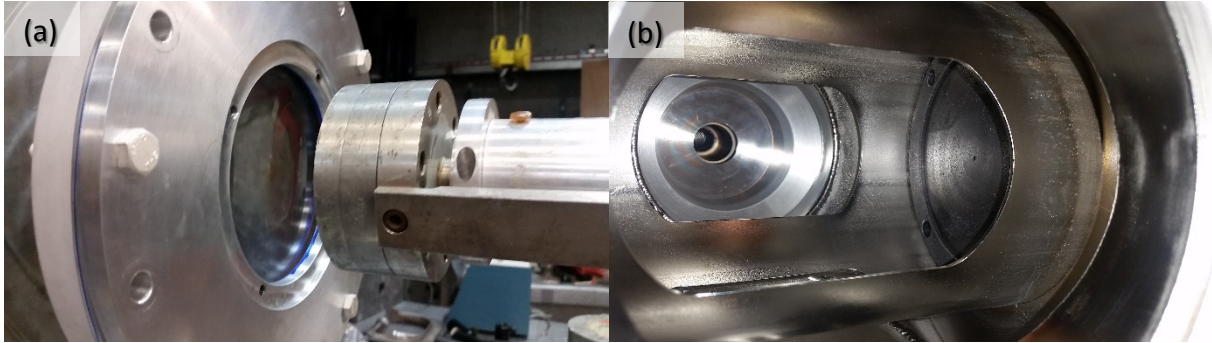

FIG. 2 (a) Front face of the experimental chamber along with accelerator exit (right). (b) Inside the chamber, looking at the back face of the graphite collimator.

The set of scintillators consisted of four materials: LYSO ($Lu_{1.8}Y_{.2}SiO_5$:Ce) , BGO ($Bi_4Ge_3O_{12}$), Bicron 422, and Bicron 404 from Saint Gobain. Each scintillator had a 1x1" cross section. The LYSO, BGO, and Bicron 422 samples were pixelated arrays of 1.5, 5, and 10 mm interaction thickness. Each of the pixels was 1x1 mm^2 and separated by 0.076 mm of white reflector paint, see FIG. 3a. The front side (facing the incoming electron beam) and edges of the arrays were also coated in the same material. The backside was left open for clean light propagation to the imaging optics. The Bicron 404 sample was cut from a larger sample with no pixels and had polytetrafluoroethylene (PTFE) tape on the front side. A Thorlabs lens mount (PN CH1A), see FIG. 3b, held the samples inside the chamber and kept the location with respect to the collimator and imaging system constant throughout the experiments.
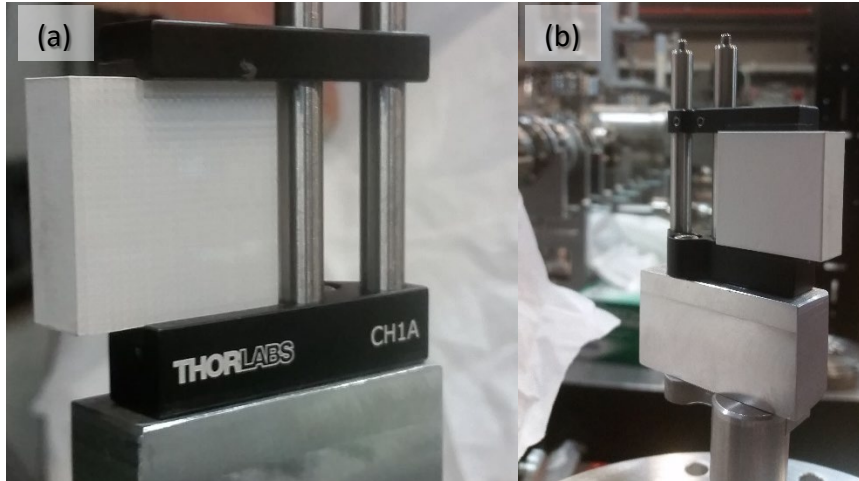
FIG. 3 (a) Back face of the 10-mm BGO array showing the 1-mm square pixels. This side faces the imaging optics. (b) Back side of the array in the target mount. This side faces the incoming electron beam.

At each energy level, a charge collector (FIG. 4) was inserted into the beamline to measure the total charge incident on the arrays. The charge collector comprised of an anodized aluminum cylinder connected in parallel with a 1-MΩ scope channel. Integrating over the duration of the signal results in the absolute charge. The 2.36" diameter, 2" long cylinder was range thick, ensuring all the electrons in the bunch are captured in the charge collector circuit.
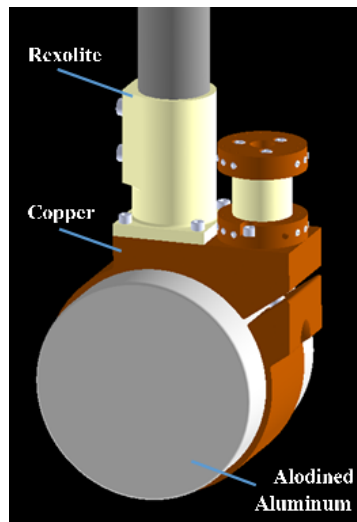

FIG. 4 Model of the charge collector.

FIG. 5 Imaging optics setup.

Shown in FIG. 5, light emitted from the scintillator arrays was directed towards a camera using a Newport 3" round mirror with UV enhanced Al coating (PN 30D20AL.2). The camera was Imaging Source DMK 37BUX273 (with a 1/2.9" Sony Pregius IMX273 sensor) outfitted with a 16-mm focal length lens (TCL1616 5MP). Metallic neutral density filters coated for minimal variation in attenuation from 250-2500-nm wavelength reduced the intensity of light on the camera sensor. The total distance the lens face to the back side of the scintillators was 19" (48 mm), giving a scale 12 pixels/mm on the images. The machine provided two triggers for every shot; the first trigger primed the linac and the second one triggered the camera. The images presented here captured the second, single pulse of the machine with an exposure time of 1 ms. Camera gain was varied to optimize the pixel intensity of the images.

3. Results and Discussion

3.1.Calibration of Charge Collector Data

The current from a non-intercepting beam monitor (NIBM) was recorded for each shot; this instrument is legacy equipment at the IAC and no extra documentation is available. Tested currents ranged from 1-45 A. The lower beam energies would not support large beam currents; Table 1 details the currents achievable at each energy. The accelerator operators read the currents off an oscilloscope signal after each shot. The charge collector allowed us to infer the total charge of the beam incident on the scintillator samples from the reported beam current. The charge collector was inserted into the beamline after removal of the scintillator sample holder. An oscilloscope recorded the voltage produced in the device as a function of time, an example of which is shown in FIG. 6. Several signals were recorded for each current and energy combination.

Beam Energy (MeV)	Tested Currents (A)
5	1, 5, 10
10	5, 10, 15, 20
15	5, 10, 15, 20, 35
20	5, 10, 20, 35, 45

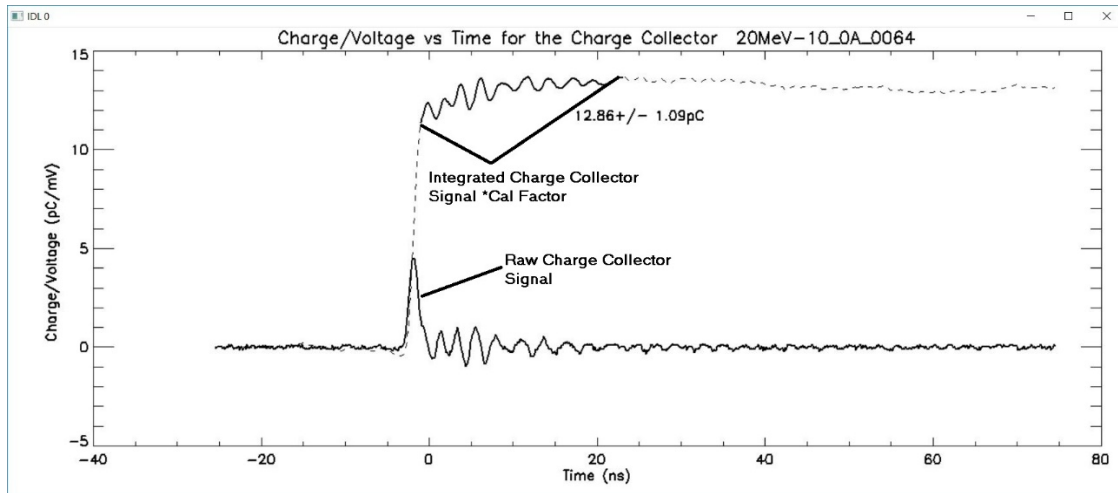Table 1 Beam currents tested at each energy

FIG. 6 Sample raw and integrated charge collector signal from a 20-MeV, 10-A electron beam. The solid lines on the integrated signal indicate averaged region.

The charge collector gives a signal that represents the deposited current, so the total deposited charge is simply the magnitude of the integrated raw signal. The calibration factor is determined by taking the average of the integrated signal over the duration of the pulse, indicated by the solid lines in FIG. 6. The results of the analysis at each energy are shown in FIG. 7. The slope of the linear fit is used as the conversion factor from beam current in A to beam charge in pC.

Beam energies of 5, 10 and 15MeV all have consistent signatures. 10 and 15 MeV have consistent calibration, while 5 and 20 MeV have very different calibrations with 5MeV at 0.17 pC/A and 20MeV at 1.7 pC/A. However, there are some major limitations to the data. Results in this report are given as a function of beam energy, current, and charge. The beam current data came from the reported NIBM. The charge was then inferred with the charge collector data. As stated above, the current was read off an oscilloscope by the accelerator operators; they simply took the amplitude of the signal and halved it. This is part of the legacy equipment issues and there is a lot of uncertainty in the reading of these numbers.

Another issue was the charge collector itself. Its design made it sensitive to any rough handling. In order to insert the charge collector, its mounting arm had to be rotated to fit it through the current return bars in the chamber. This put a strain on the cables attached to the resistor tower (right hand side of FIG. 4); these resistors are held in electrical contact with setscrews to facilitate changing the total resistance during testing. However, the mechanical structure was not sound and we had issues getting the resistors to remain in solid contact with the body. It is highly likely that the circuit was not connected at all times during our experiments. Several shots were taken at each data point to verify beam and charge collector stability. The most variability in the calibration results occurred at 20 MeV. The signals have a different structure on the day they were taken; further indicating damage being done during insertion/removal of the charge collector.
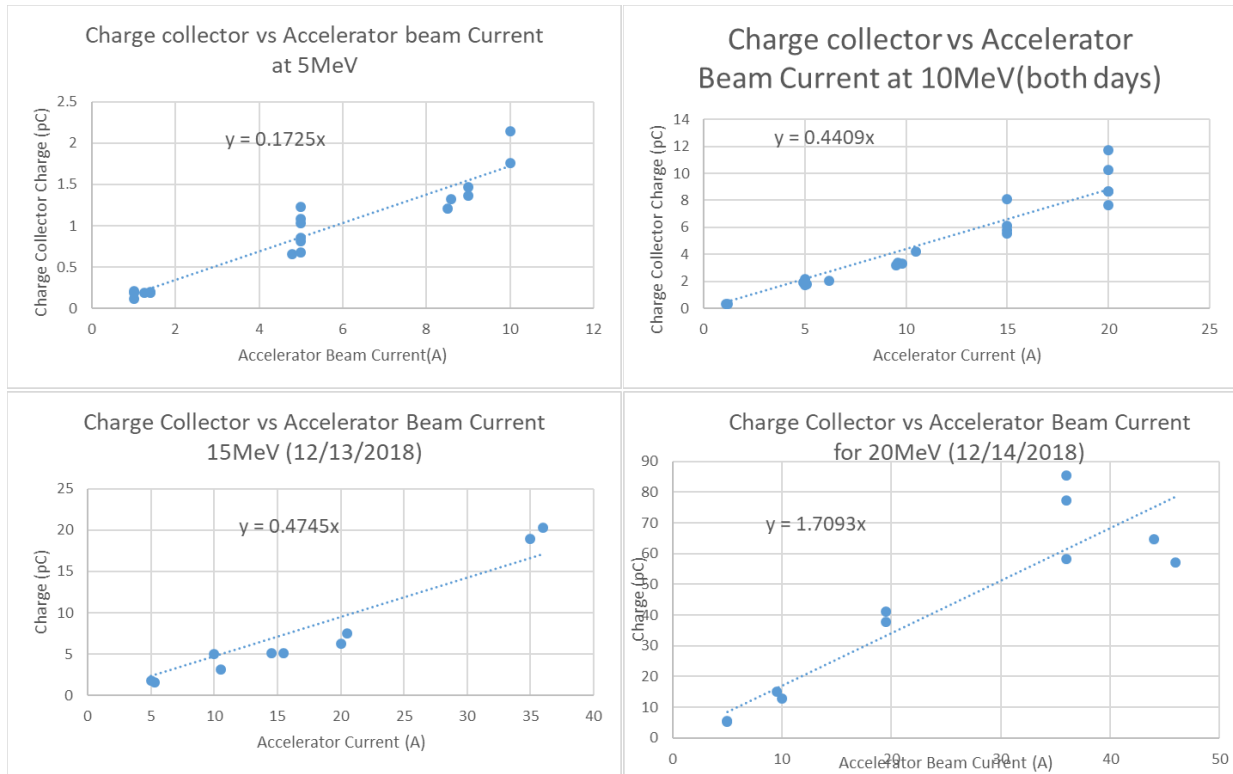
FIG. 7 Charge collector calibration data at each beam energy. The conversions from current to charge are 0.1725, 0.4409, 0.4745, and 1.709 pC/A.

3.2. Relative Response of Scintillators

3.2.1. Analysis Method

Each sample image is captured with a record of accelerator current as reported by the NIBM, charge measured with the Bergoz monitor (which is discarded), gain setting of the camera (in dBm), and the neutral-density of the filters in front of the lens. All images are incrementally numbered and logged. Candidate images with good image quality are identified for each sample, energy, and current setting to analyze. All images are cropped by 50% relative to the image center plus an offset to approximately center the cropped image on the beam spot to avoid bright objects in the scene.
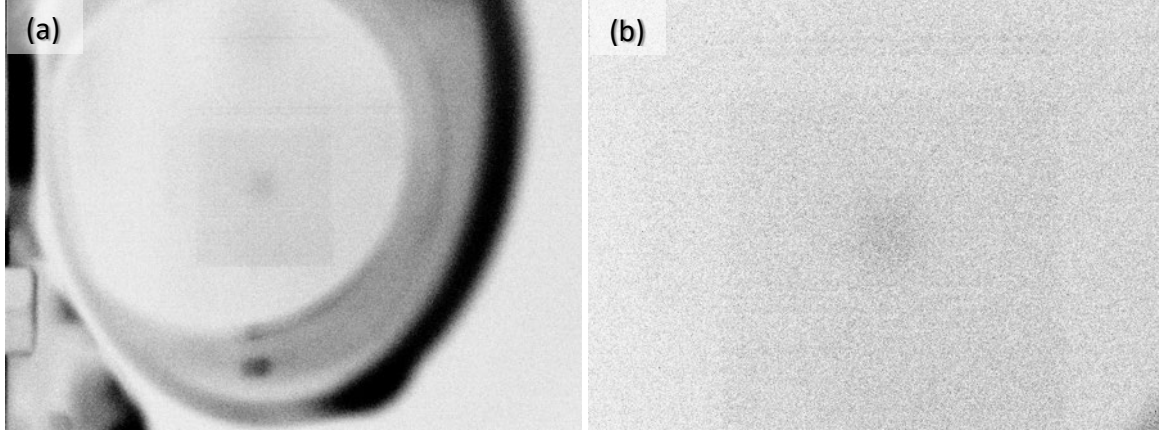
FIG. 8 (a) Original vs. (b) cropped image for an especially dim shot (number 82). Images are inverted for visibility.

To derive the sample intensity for a given sample image, first a peak finding algorithm identifies the approximate center of the beam spot. After subtracting background in a fitting region around the spot center and converting to floating point, a two-component 2D Gaussian function is fitted to the peak with a functional form

$$A\exp\left(\frac{(x-x_1)^2}{2\sigma_{x1}^2}-\frac{(y-y_1)^2}{2\sigma_{y1}^2}\right)+B\exp\left(\frac{(x-x_2)^2}{2\sigma_{x2}^2}-\frac{(y-y_2)^2}{2\sigma_{y2}^2}\right)$$

so that the two Gaussian components have independent centroids to account for asymmetry in the beam spot. The fitted Gaussian is used to generate a test image in floating point with dimensions large enough to capture the model fully, which is then divided by the camera gain for the shot. This image is integrated over a region where the fitted model is above a specified threshold. This integral is taken to be the raw intensity for the shot. FIG. 9 shows the fitting outputs from a typical shot in both image space and in X and Y lineouts through the spot peak. The raw image in FIG. 9(a) is fitted with the 2D Gaussian shown in FIG. 9(b), whie FIG. 9(c) shows the residual image formed by subtracting the fitted Gaussian from the original image. FIG. 9(d) shows the summed X and Y lineouts around the peak along with the Gaussian fit.

An important phenomenon affecting the fitted intensity is the difference between the intensity in the scintillator pixels and the "grid" formed by the interstitial reflective coating. For some samples and beam energies, the grid is dimmer than the scintillator pixels like in shot 543 of BC-422 at 15 MeV in FIG. 9. The dips in FIG. 9(d) show the dimmer interstitial grid, and as a result the effective peak intensity is reduced slightly. For BGO and especially at lower energies the opposite can occur, with the interstitial grid appearing brighter than the scintillator pixels as shown in FIG. 10 for BGO at 10 MeV, increasing the fitted peak intensity above baseline. We do not address this in the current analysis.

The raw intensity does not account for any ND filters inserted for the shot, nor for the differences in emission spectra vs. wavelength between the different sample materials convolved with the sensitivity of the optical elements. Deconvolving both effects requires reasonably accurate models of the scintillator emission spectra and all optical elements. Saint-Gobain provides plots of approximate emission spectra in its scintillator specification sheets, shown in FIG. 11. These spectra were digitized using DataThief, then smoothed, interpolated to a common wavelength grid, and normalized. The digitized scintillator spectra used for modeling optics response is shown in FIG. 12. The wavelength range used for modeling is from 340 to 700 nm, though the highest emission data cuts off around 640 nm.
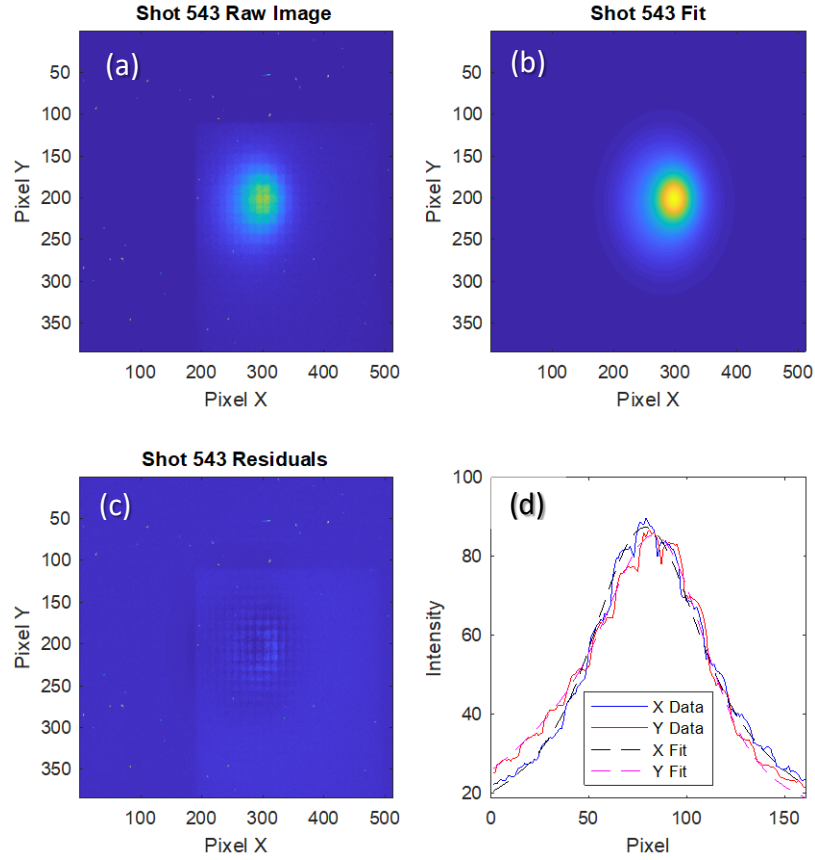
FIG. 9 Example fitting routine data for a shot image. (a) Input cropped image, the scintillator array is faintly visible and individual pixels are evident. (b) Image generated from Gaussian fit to image peak. (c) Residual image after subtracting Gaussian fit from raw image. (d) X and Y lineouts in region around peak showing data and Gaussian fit. This shot has a small amount of asymmetry as well as some errors from the darker interstitial reflector grid, but the overall fit is acceptable.
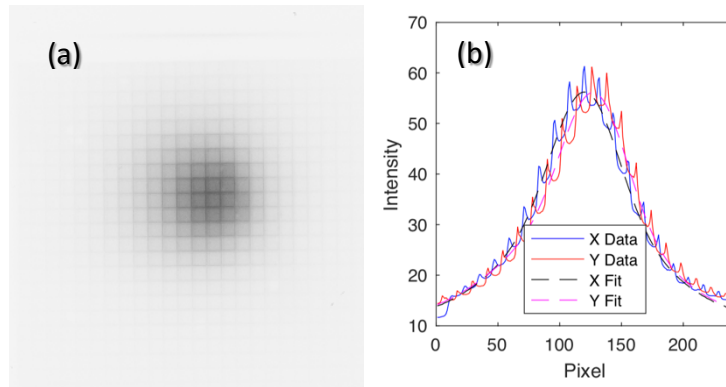

FIG. 10 Example of BGO image showing bright pixel interstitial elements. (a) Cropped inverted image of shot 450: the darker grid lines in this image are brighter than the pixels in the original. (b) The fitted X and Y lineouts show spikes at the interstices, increasing the amplitude of the fit above the baseline established by the pixels themselves.
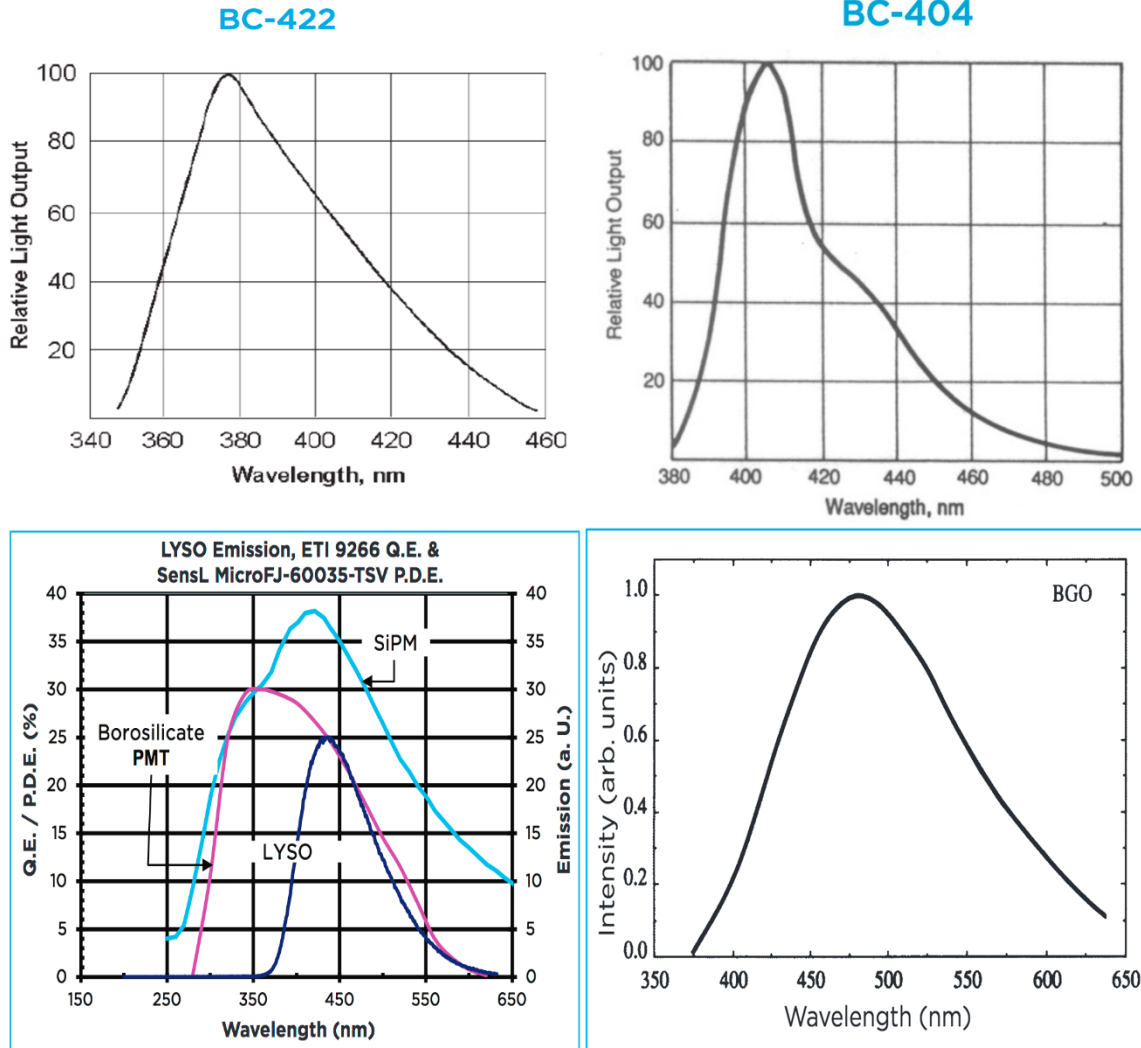
FIG. 11 Scintillator emission spectra provided by Saint-Gobain. Some plots do not show the full spectrum down to 0% intensity.

Efficiency data for the optical elements were acquired from the manufacturers in a similar fashion, including the quantum efficiency of the camera sensor (from https://thinklucid.com/product/phoenix-16-mp-imx273/), the transmission of the lens, and the reflectivity of the mirror. The mirror data is the most uncertain, as the Newport only has data covering the ranges 250-600 nm and > 1000 nm for the AL.2 mirror. The range from 600 to 700 nm was approximated by merging in a rescaled version of the Al2_AO18 reflectance plot "AL2_AOI8_600w.gif" found at https://www.newport.com/p/30D20AL.2 with the standard AL.2 plot "AL.2_600w.gif" found on the same page. The Mylar transmission data is approximated with the 90D transmission curve from http://usa.dupontteijinfilms.com/wp-content/uploads/2017/01/Mylar_Optical_Properties.pdf. This transmission curve for 23 μm-thick film underestimates the total attenuation due to the Mylar, but we are interested in the general shape of the transmission curve with respect to energy so it suffices here. The ND filter data was scanned and converted from the measured transmission data supplied by the manufacturer with the optics. The interpolated efficiency curves used for these calculations are shown in FIG. 13. Some samples were

measured with the OD = 1.0 and OD = 0.5 filters stacked for a combined OD of 1.5, this curve is calculated from the OD = 1.0 and 0.5 curves.
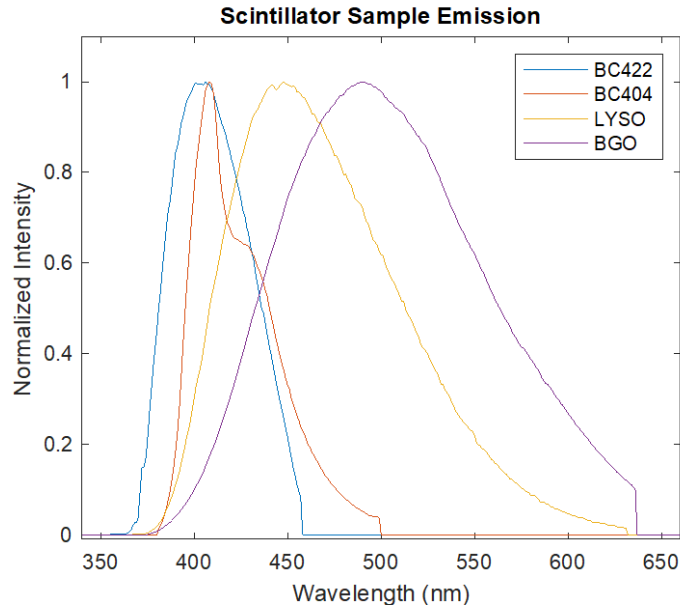

FIG. 12 Emission spectra data used for modeling ND filter and optical response. The data is traced from emission spectra plots provided by the manufacturer.
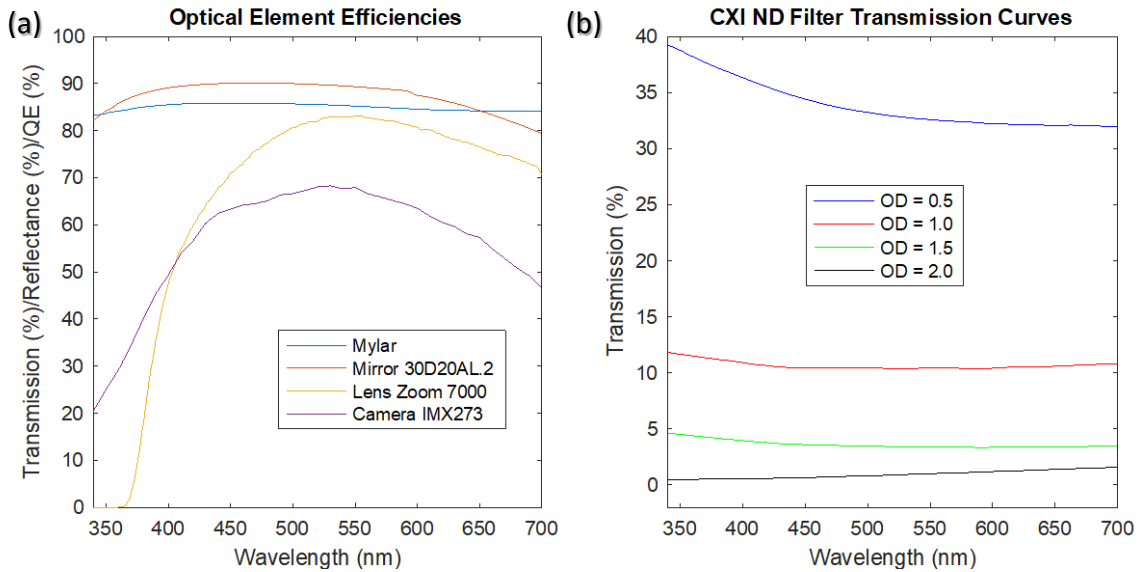

FIG. 13 Efficiency data for optical elements. (a) Transmission/reflectance/quantum efficiency of static optical elements (present for all shots). (b) Transmission data for the ND filters

These efficiency and emission data were combined to calculate two, sample-dependent scaling factors, one for the OD of the filters and another for the transmission/absorption curve through the static optical elements. To compute the ND filter factor, the normalized emission spectrum is multiplied element-wise by the transmission of the ND filter, integrated, and finally divided by the original integral

of the normalized spectrum. Dividing the fitted image raw intensity is by the ND filter scale factor yields an intensity that has removed the effect of ND filters for that shot, termed the ND-scaled intensity. A similar calculation is performed for the four sample types convolved with the four static optics elements present in every shot (Mylar window, mirror, lens, and camera optic), integrated, and divided by the normalized spectrum intensity to yield the sample emission scale factor. Dividing the fitted image raw intensity by both the sample scale factor and ND scale factor yields the best approximation to the true intensity and is termed the "absolute intensity". The absolute intensity is used to compare relative brightness of different samples. Table 2 lists the computed sample and ND filter scale factors.

Sample	Sample Scale Factor	OD	ND Scale Factor
BC-422	0.1239	0.5	0.3673
		1	0.1105
		1.5	0.0406
		2	0.0055
BD-404	0.2431	0.5	0.3562
		1	0.1071
		1.5	0.0382
		2	0.0059
LYSO	0.3308	0.5	0.3440
		1	0.1054
		1.5	0.0363
		2	0.0071
BGO	0.3753	0.5	0.3357
		1	0.1047
		1.5	0.0351
		2	0.0083

Table 2: Calculated scale factors for sample transmission through ND filters and static optical elements.

3.2.2. Scintillator Response vs Charge

These first plots (FIG. 14 through FIG. 20) show the absolute intensity (deconvolved sample scale factors and ND filter scale factors) for each sample plotted vs. pulse charge at the four measured beam energies (5, 10, 15, 20 keV). As noted in the previous section, the absolute intensity is the best estimate of the true light output from the scintillator with the instrument response removed. The beam charge is calculated from the reported beam current using the calibration derived from the charge collector analysis (see Section 3.1). Each energy series (e.g. 5 MeV) has been fitted to a power law model of the form Ax^B, with the fit coefficients A and B shown in the figure legend. The first (lowest-charge) point in each series is omitted for the fit due to data quality problems noted in the conclusions on page 15.
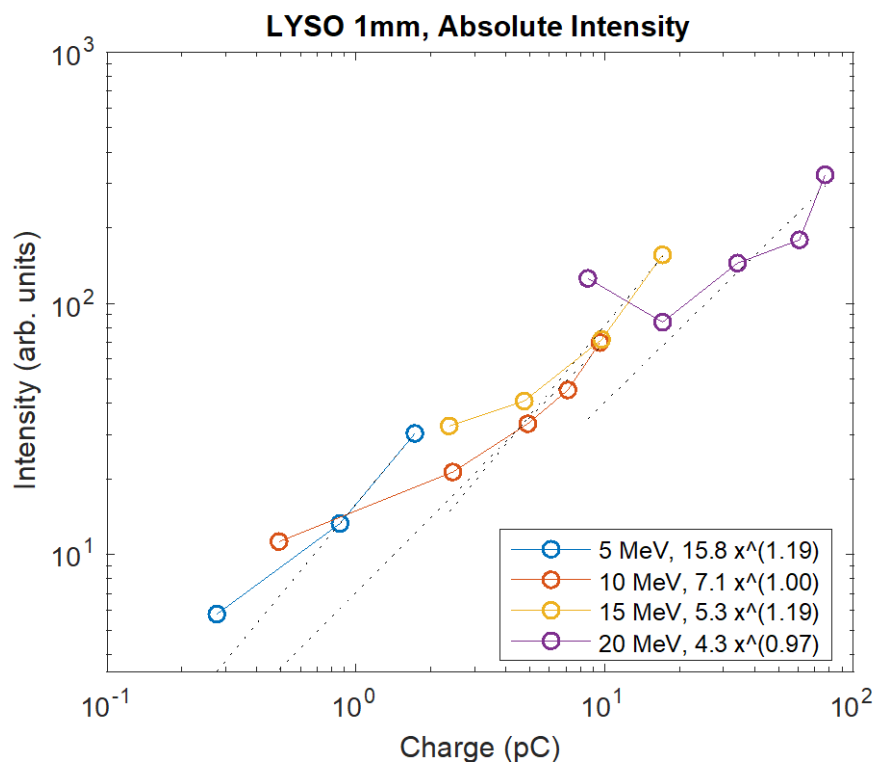
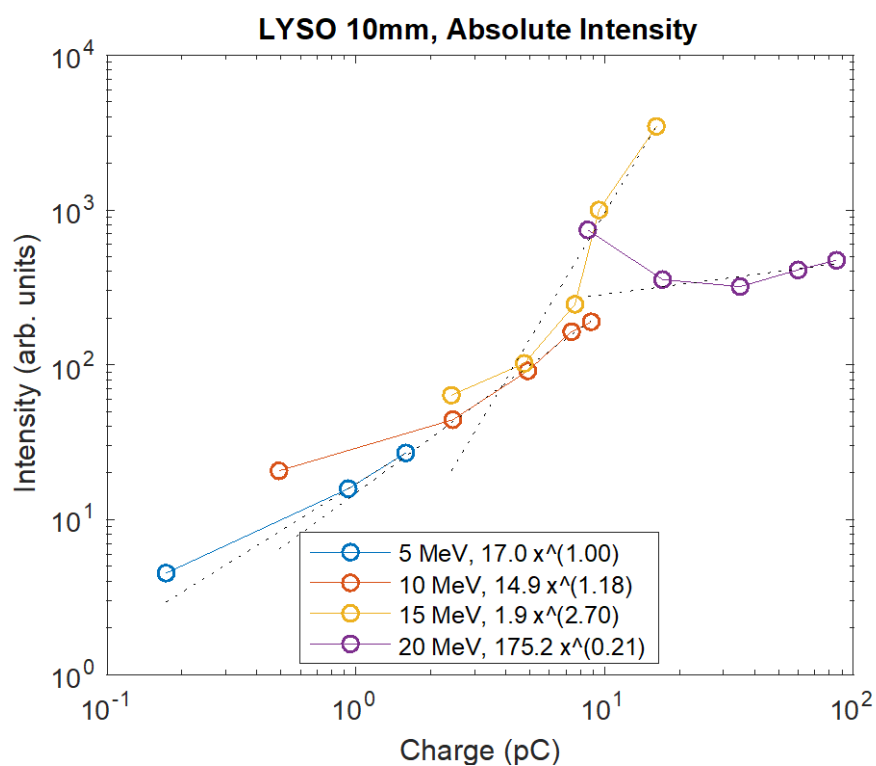FIG. 14 Intensity vs. Charge for LYSO at 1 mm thickness.

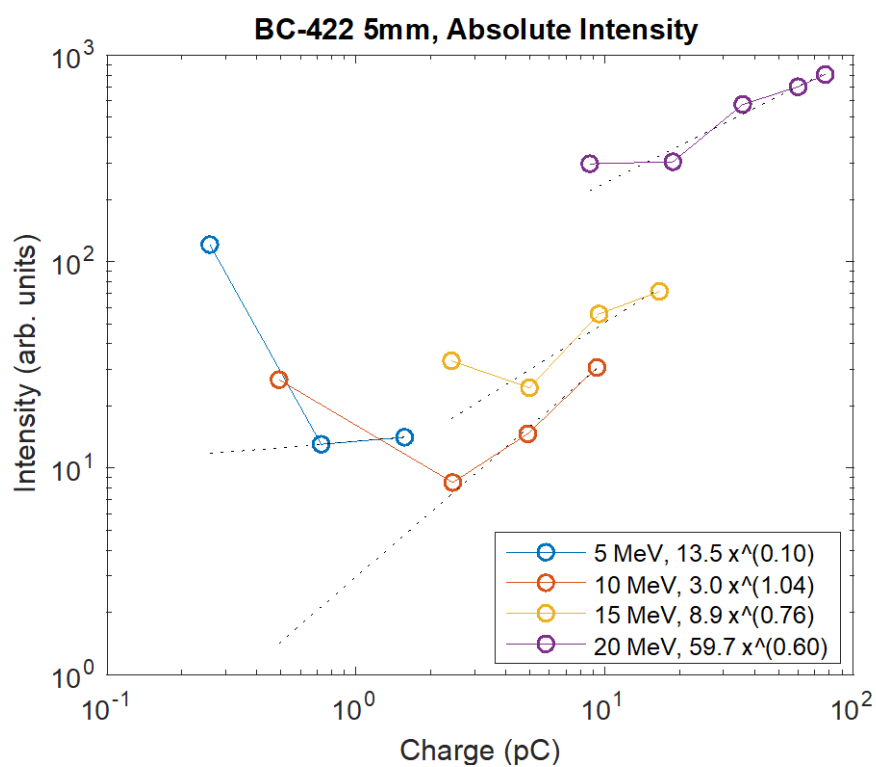FIG. 15 Intensity vs. Charge for LYSO at 10 mm thickness.

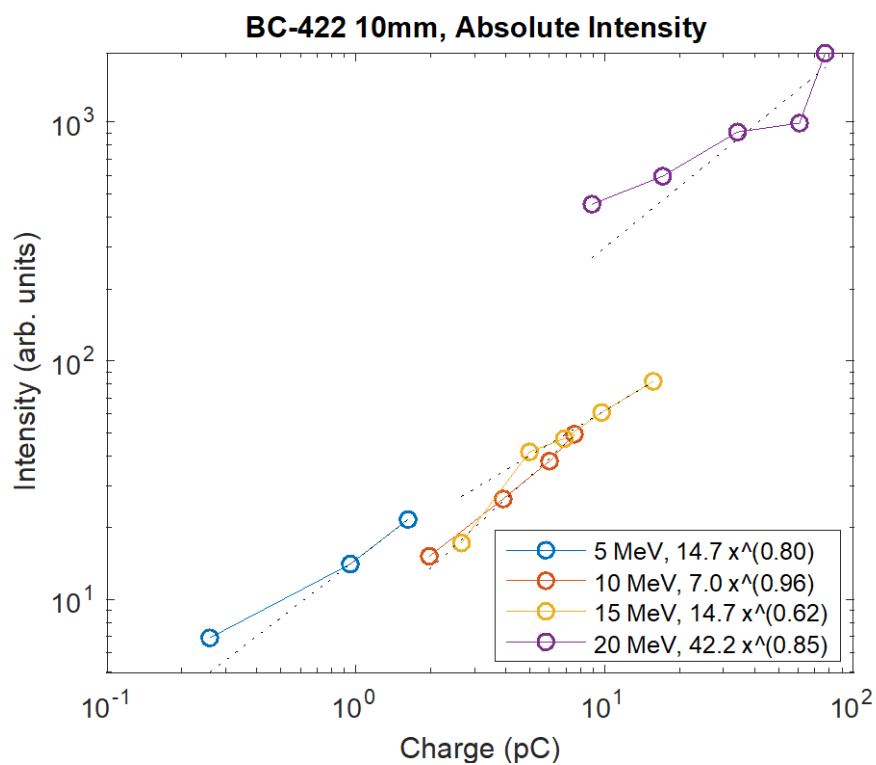FIG. 16 Intensity vs. Charge for BC-422 at 5 mm thickness.

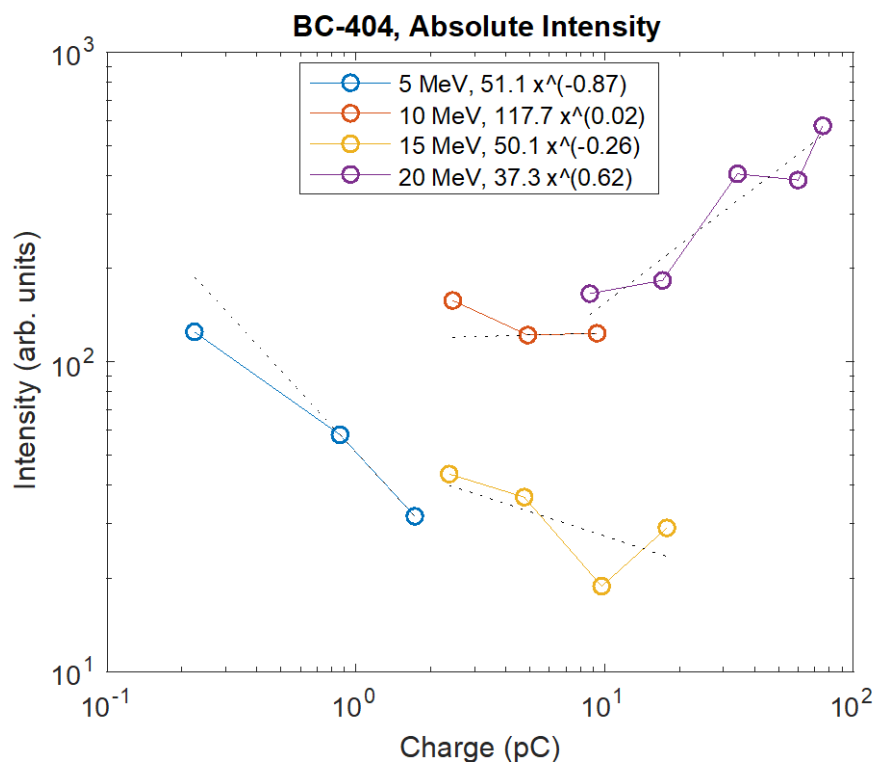FIG. 17 Intensity vs. Charge for BC-422 at 10 mm thickness.

FIG. 18 Intensity vs. Charge for bulk BC-404 at 4.5 mm thickness, wrapped on the front side with PTFE tape.
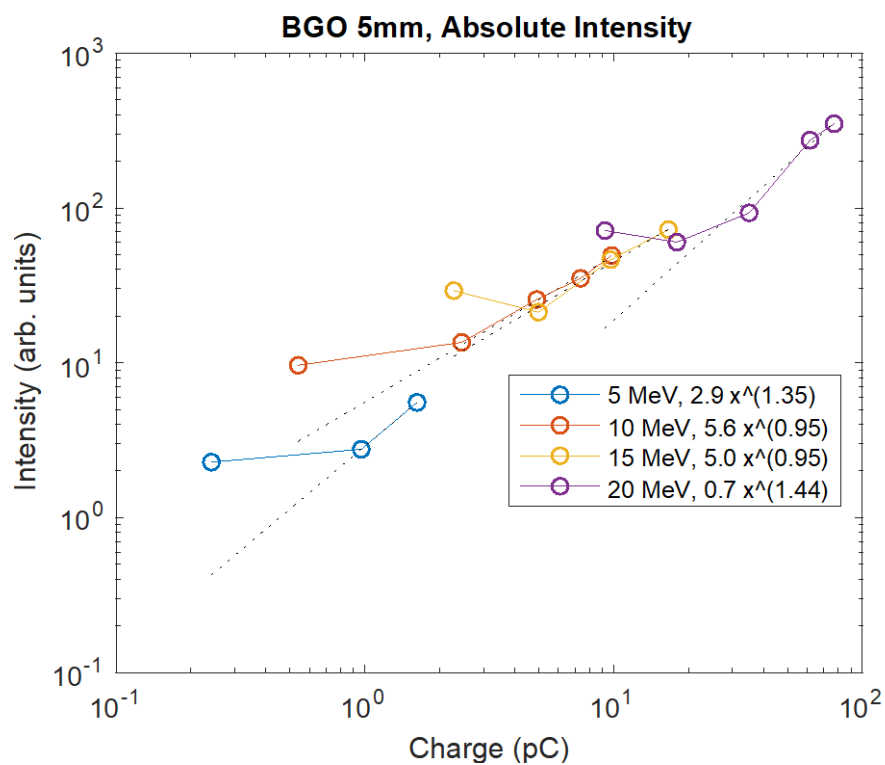

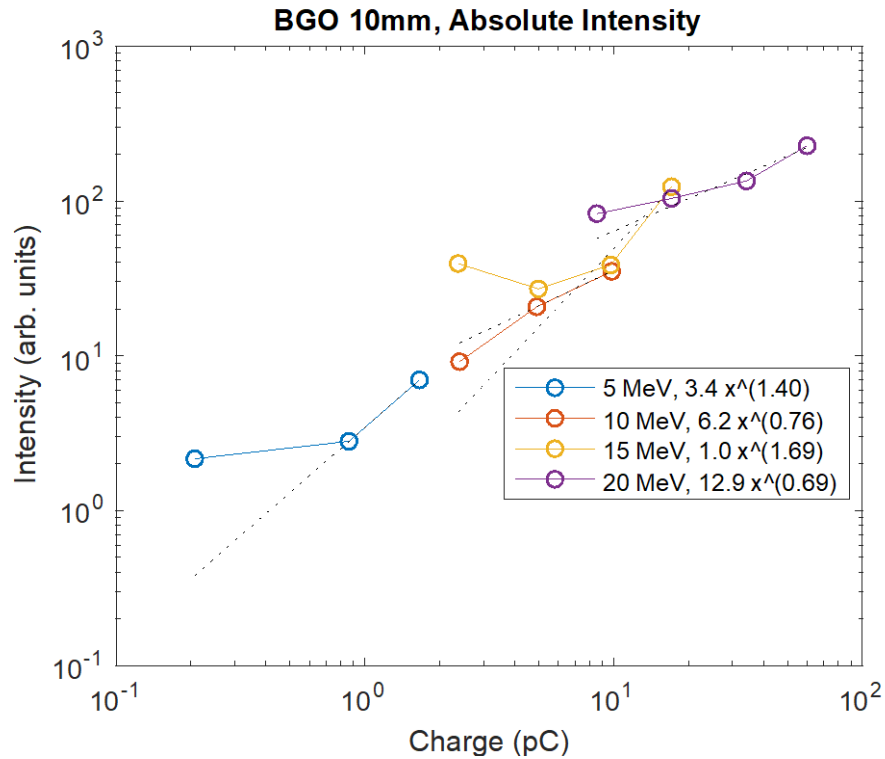FIG. 19 Intensity vs. Charge for BGO at 5 mm thickness.

FIG. 20 Intensity vs. Charge for BGO at 10 mm thickness.

We can make some general conclusions from these plots (and the data that produced them):

1) The 20 MeV data is of lesser quality than the other three beam energy data sets. There is greater variation among the sample intensities at that energy and in the reported beam current used to calculate the pulse charge. This agrees with our experience during the 20 MeV run: the machine was operating with less stability.

2) The lowest-charge data point in each energy series is often an outlier. This first-point error is not unexpected given the accelerator is operating at its lowest possible beam current and may be less stable compared to currents in the middle of its range. This data point is omitted for analysis.

3) The 5 mm BC-422 and BC-404 samples (FIG. 16 and FIG. 18) show large variation. The BC-422 sample may be marginal if we account for the first-point error and some variation in the 20 MeV data. The BC-404 data is poor and inconclusive.

4) The remaining samples show reasonable linearity in log-log space, with the exception of the lowest-charge point in each energy series. This implies that the beam energy is fully deposited in the scintillators and the brightness is only dependent on the total number of electrons.

The power law fit parameters allow more specific analysis within the limitations of this data quality. The response of scintillators to energetic electrons is expected to follow a form $I = A(E)Q$, where I is the intensity (number of photons produced), $A(E)$ is a scale factor dependent on the incident electron energy, and Q is the charge/number of electrons in the pulse. Ideally, the brightness depends linearly on

the charge deposited, so the exponent B in the fit Ax^B would equal 1. Large deviation from 1 in the exponent can suggest multiple issues: 1) less than 1 suggests saturation effects in either the scintillator or detector; 2) greater than 1 suggests nonlinear detector response; or 3) either < 1 or > 1 could be from bad control of experiment systematics and amplified noise, or other similar issues. The fitted scale factor A should be proportional to the scintillator response at the fitted energy, but it is correlated with the fitted exponent so it is not a totally reliable metric. For fitted exponents close to the expected value of 1 we expect the fitted factor A to be a good approximation to the scintillator response, but for fits with large deviation from B = 1 we consider the fit to be wrong and should not draw a conclusion from either coefficient.

With these caveats in mind, Table 3 lists the fitted exponent values for each energy series of all samples as shown in the legends in FIG. 14 through FIG. 20, along with the average of the fitted exponents for all energy series for a given sample. To distinguish good exponent fits from bad fits, we declare that values between 0.8 and 1.2 are "good" and those outside that interval are "bad", with bad values formatted with a strike through the text. Some samples stand out immediately as poor such as BC-404 and 10 mm BGO, while 1 mm LYSO and 10 mm BC-422 have more acceptable fits and the remaining three samples are mixed. This falls in line with the general conclusions and the scatter in the data presented in FIG. 14 through FIG. 20.

	LYSO 1mm	LYSO 10mm	BC-422 5mm	BC-422 10mm	BC-404	BGO 5mm	BGO 10mm
5 MeV	1.19	1.00	0.10	0.80	~~-0.87~~	~~1.35~~	~~1.40~~
10 MeV	1.00	1.18	1.04	0.96	~~0.02~~	0.95	~~0.76~~
15 MeV	1.19	~~2.70~~	~~0.76~~	~~0.62~~	~~-0.26~~	0.95	~~1.69~~
20 MeV	0.97	~~0.21~~	~~0.60~~	0.85	0.62	~~1.44~~	~~0.69~~
Average	1.09	~~1.27~~	~~0.63~~	0.81	~~-0.13~~	1.17	1.14

Table 3: Fitted power law exponents for each sample. These are the B coefficients in the fitted power law $A\ x^B$ shown in the legends in FIG. 14 through FIG. 20. Values outside of the interval [0.8,1.2] are considered bad and are formatted with a strikethrough.

Table 4 lists the corresponding fitted power law A coefficients for all samples, with "bad" data points struck through as in Table 3. The strikethrough is based on the corresponding B coefficient shown in Table 3. For the remaining good data points we observe a decreasing trend with energy in 5 of the 7 samples, in good agreement with the typical response curve in Morneau's work which has a maximum around 5 MeV followed by decreased energy deposition and response. These coefficients are only proportional to the response and do not give absolute light output (e.g. in photons per particle per MeV). Despite the issues and holes in the data set these results are promising for follow-up measurements.

	LYSO 1mm	LYSO 10mm	BC-422 5mm	BC-422 10mm	BC-404	BGO 5mm	BGO 10mm
5 MeV	15.8	17.0	13.5	14.7	~~51.1~~	~~2.9~~	~~3.4~~
10 MeV	7.1	14.9	3.0	7.0	~~117.7~~	5.6	~~6.2~~
15 MeV	5.3	~~1.9~~	~~8.9~~	~~14.7~~	~~50.1~~	5.0	~~1.0~~
20 MeV	4.3	~~175.2~~	~~59.7~~	42.2	~~13.2~~	~~0.7~~	~~12.9~~

Table 4: Fitted power law scale factors for each sample. These are the A coefficients in the fitted power law $A\ x^B$ shown in the legends in FIG. 14 through FIG. 20. Values for which the B exponent is outside of the interval [0.8,1.2] are considered bad and are formatted with a strikethrough.

The next plots (FIG. 21 through FIG. 23) are essentially the same as in FIG. 14 through FIG. 20, with all samples of a given material on the same plot to show variation among different thicknesses of the same sample. There is good overlap in the observed intensity at different thicknesses over all energies, demonstrating general insensitivity to sample thickness.
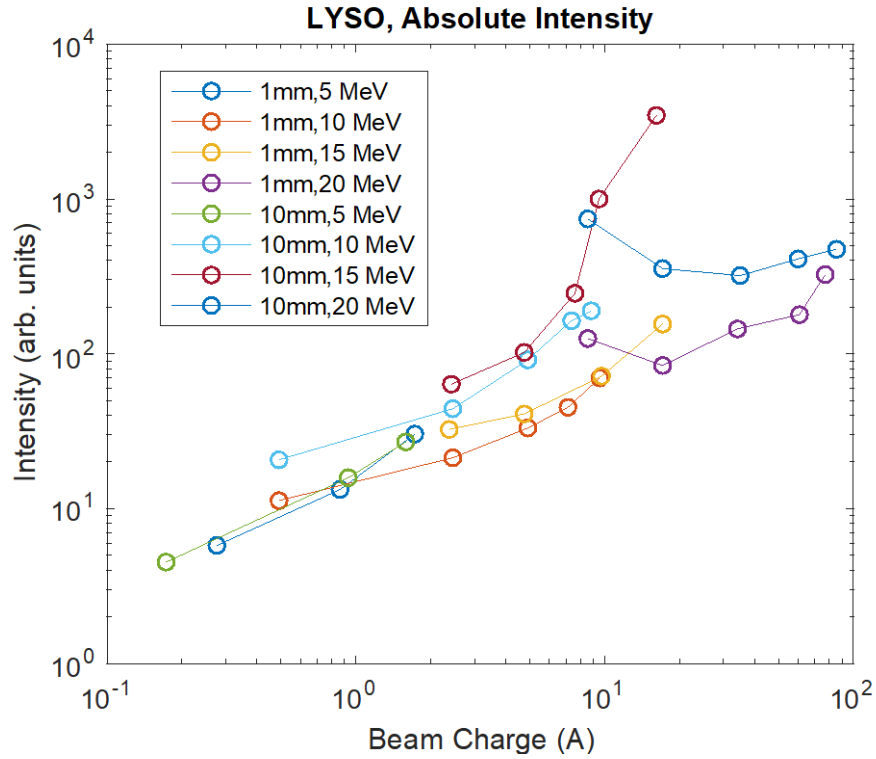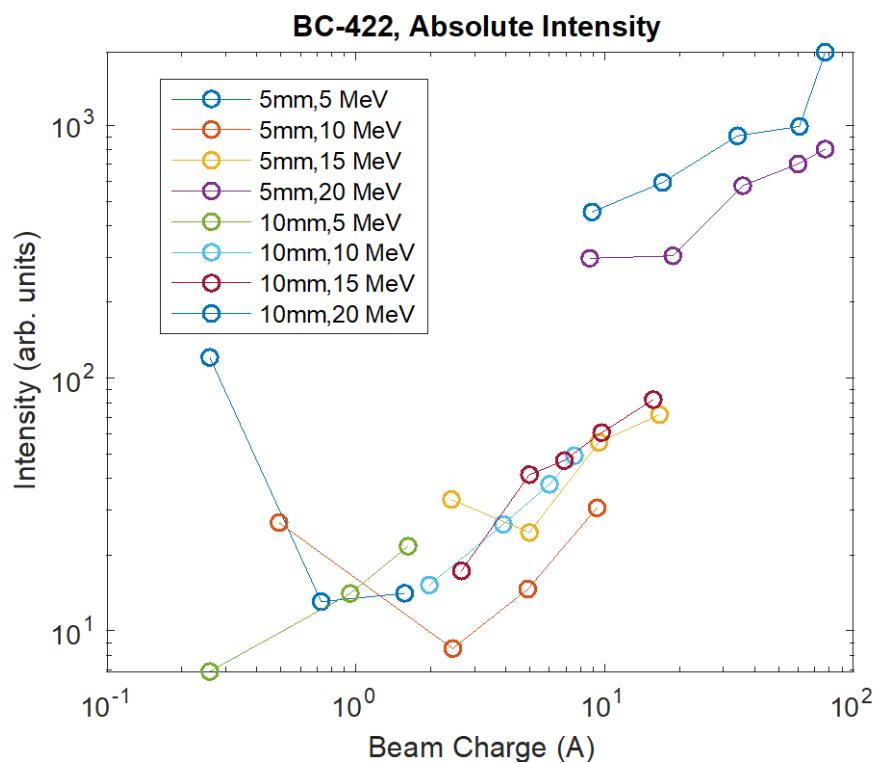

FIG. 21 Intensity vs. Charge for LYSO.
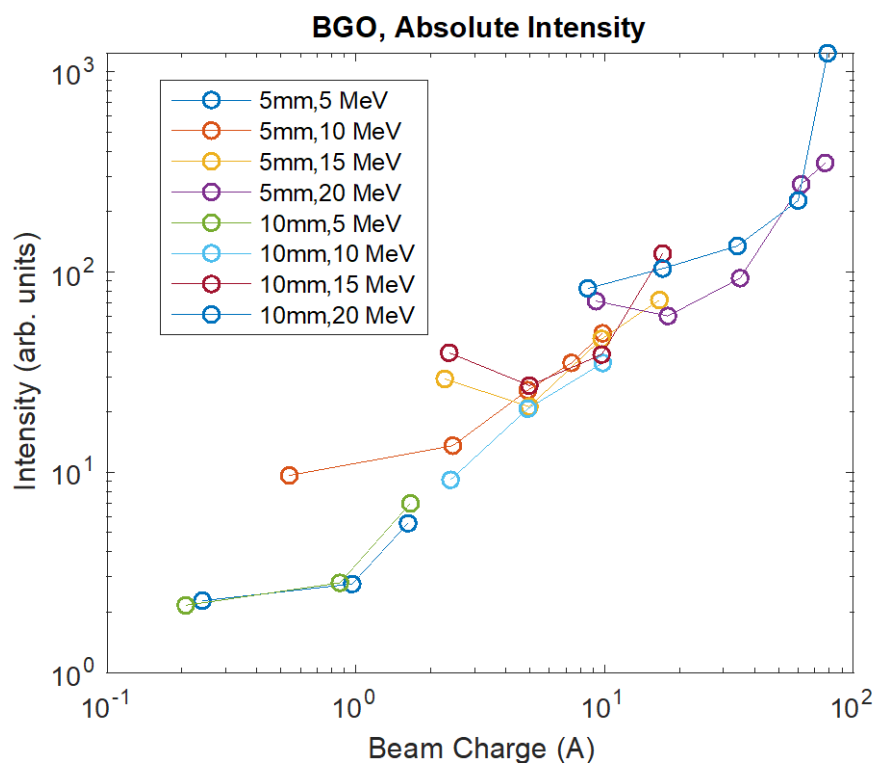
FIG. 22 Intensity vs. Charge for BC-422.

FIG. 23 Intensity vs. Charge for BGO.

3.2.3. Scintillator Response vs. Energy

The plot in FIG. 24 shows the absolute intensity of all samples as a function of beam energy at a beam current of 10 A. These data points at different beam energies are not directly comparable to one another (e.g. between 5 and 10 MeV beam energy) because the pulse charge changes as a function of beam energy in addition to beam current. So, the highest beam current at 5 MeV has much less charge than the lowest beam current at even 10 MeV, and there is no beam current that allows for the same charge at each energy. This plot illustrates the relative brightness of the samples compared to one another and how that scales with energy.

It is difficult to extract solid trends from this plot. The samples are relatively close to one another without consistent winners in brightness. BC-422 samples had anomalously high brightness at 20 MeV, and the BC-404 data should be discarded. LYSO is generally brighter than the other samples except for at 20 MeV, and BGO is generally dimmer. Adding to this conclusion is the variation among interstitial brightness discussed earlier in reference to FIG. 10: the BGO samples tend to have brighter interstices and the fits are over estimating their brightness, while the other samples typically have dim interstices and are under-estimated in brightness. Therefore, it is safe to conclude that BGO is the dimmest material tested.
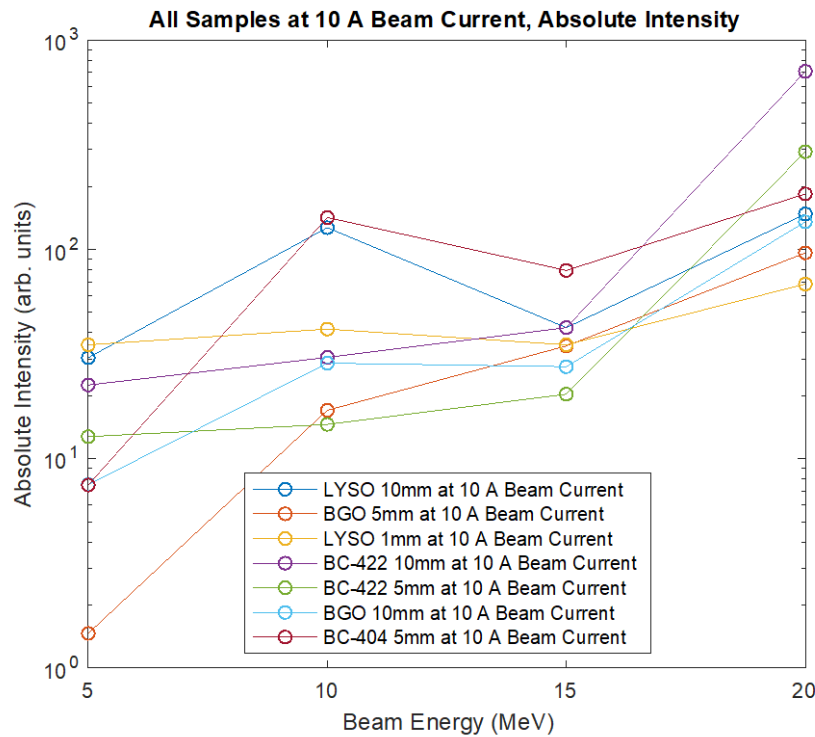

FIG. 24 Intensity vs. Energy sample comparison at 10 A beam current.

3.3. Spot Size Variations

The emitted spot sizes were investigated as a function of beam energy, beam charge, and scintillator thickness and material. Each image was cropped to only include the scintillator; for example, see the blue box in FIG. 25a. We then integrate the image in both the x- and y-direction to get the pixel intensity as a function of position along the scintillated spot. This is the black trace on the X and Y integral

graphs below. Next, a background region is selected and integrated (red boxes), giving the red trace on the graph. Finally, the blue trace is the difference between the two.
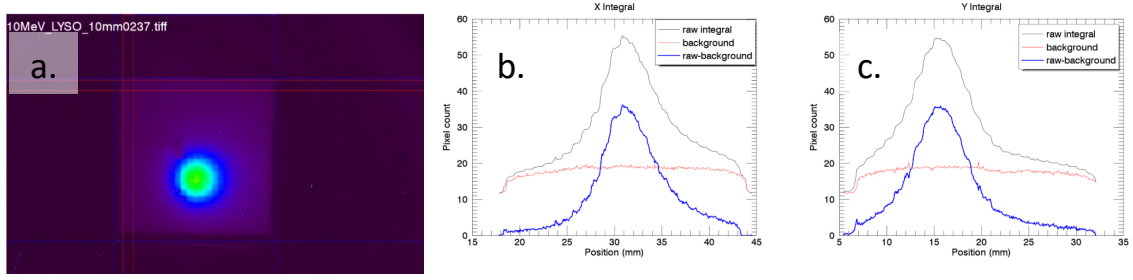

FIG. 25 (a) Cropped, false-color image of the 10-mm LYSO struck by a 10-MeV, 20-A electron beam. The blue lines indicate x and y regions of the integral and the red lines show the regions selected for background subtraction. The x and y integrals and their difference are shown in (b) and (c), respectively.

The shape of the spots is roughly Gaussian (FIG. 26). The 3-parameter gaussian fit is of the form

$$f(x) = A_0 e^{-z^2/2}; \; z = \frac{x - A_1}{A_2},$$

which is a simple Gaussian with transverse offset and the full width half maximum (FWHM) of the distribution is $2A_2\sqrt{2\ln 2}$. However, note the higher tails that are not always capture by the fit; so the fit tends to underestimate the size of the spot. For example, consider the x and y sizes reported in FIG. 26b and c. They show the FWHM of the Gaussian fit and the root-means-squared (RMS) sizes of the spot. The RMS spot size is given by

$$\langle x^2 \rangle = \frac{\sum_i w_i * (x_i - \bar{x})^2}{\sum_i w_i}$$

$$\bar{x} = \frac{\sum_i w_i * x_i}{\sum_i w_i}$$

where w_i is the pixel count or intensity of the pixel located at location x_i (or y_i for the other direction), $\bar{x}$ is the first moment, or centroid, of the distribution. The RMS spot sizes are 4.23 and 4.54 mm, while the RMS width of the Gaussian fit, from 7.79 and 7.67 mm FWHM, are 3.31 and 3.27 mm. The RMS spot size is not as sensitive to distribution shape as the Gaussian fit method. The centroid values reported on the image are the RMS centroids, $\bar{x}$.
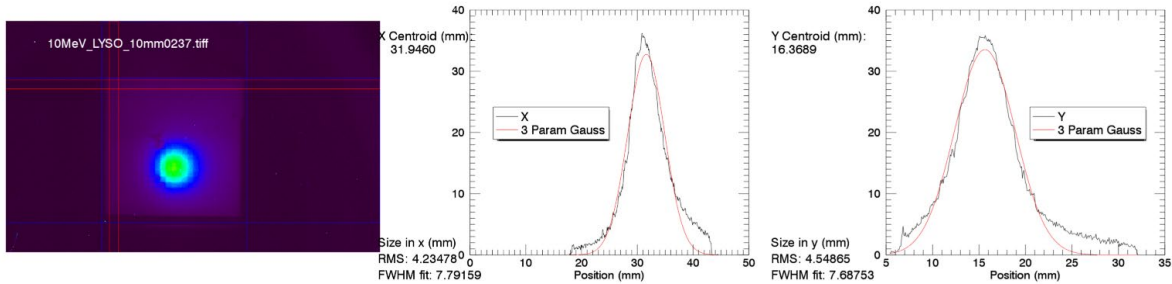

FIG. 26 (a) Identical image to FIG. 25a. (b) and (c) show the background selected integrals in x and y, respectively, and their associated Gaussian fits. The centroid values are the RMS centroids. The sizes of the two methods is shown to the bottom left of each plot. The associated RMS widths of the Gaussian fits are $(2\sqrt{2\ln 2})^{-1} \approx 0.42$ times the FWHM, giving 3.31 and 3.27 mm for the x and y sizes.

3.3.1. Spot sizes at each energy

Below is a summary of spot sizes for each energy as a function of charge on the scintillator (FIG. 27). The current recorded from the NIBM was converted to charge using the fit function determined in Section 3.1. Several shots at each energy, thickness, current and material were averaged to determine spot size at given charge. The vertical and horizontal error bars represent the standard deviation of the spot size and charge for a scintillator sample and requested current. The y-axes of the plots are the same across the x- and y-RMS spot size plots in FIG. 27.

For beam energies of 10, 15, and 20 MeV, the spot size remains constant with charge. However, some deviations begin at the lower charge end of 10 MeV. At 5 MeV, note the large deviation for the 1- and 5-mm BGO (and 10-mm for the y-RMS size) and the BC404 samples. The spot size drastically increases as the beam charge decreases. This is likely due to crosstalk between the pixels and scattering of electrons and photons within the scintillator itself as discussed in Section 3.2.1. In the other energy regions, BGO actually results in the smaller spot sizes, while the BC404 exhibits the largest. This could be due to the material properties (photon and electron scatter) or the lack of pixels in the BC404. It is more likely due to the increased scattering of photons in the material. The white paint separating the pixels serves only to direct the emitted photons towards the back face of the scintillator; it should not affect the electron energy deposition.
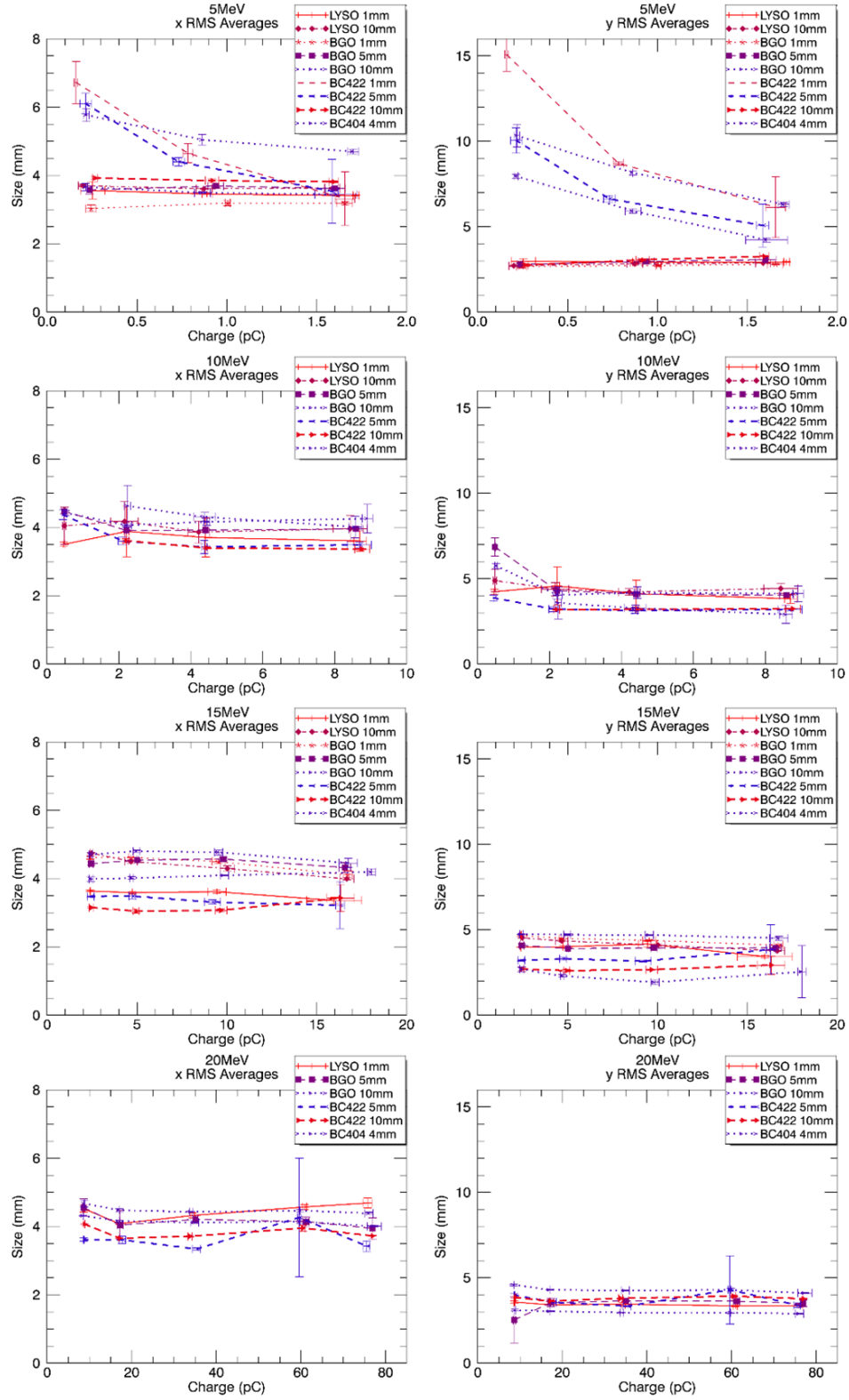
FIG. 27 Emitted RMS spot sizes as a function of charge at each energy. The top line presents the spot sizes in the x-direction and the bottom line presents the y-direction. Error bars are the standard deviations in the spot size and charge.
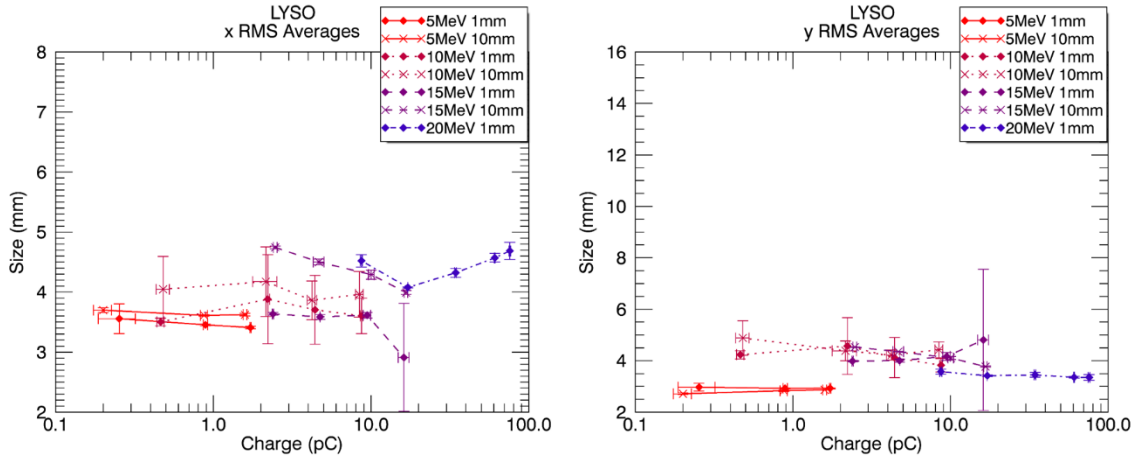
FIG. 28 LYSO RMS spot sizes

The LYSO results are shown in FIG. 28. There were no data for 20-MeV energy, 10-mm LYSO. In general, the 10-mm LYSO sample smaller spot sizes than the 1-mm sample. At similar beam charge, the higher energy electrons produce a larger spot. These differences are smaller for the y-spot size. Spot size is relatively independent of beam energy and charge.
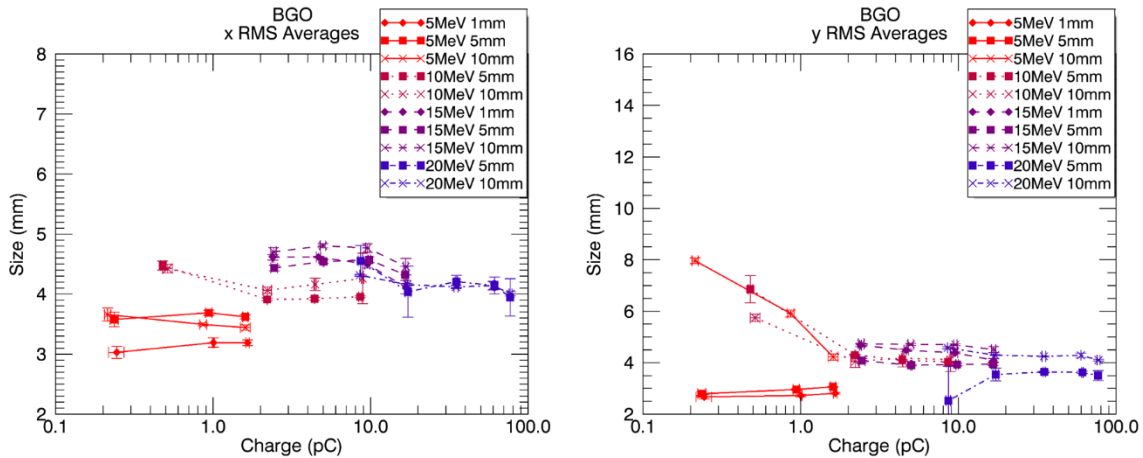

FIG. 29 BGO RMS spot sizes

The BGO results are shown in FIG. 29. Again, the higher energy beam and thicker samples produce a larger spot for the same deposited charge. Spot size does not change with beam charge. The spot size has little variation between 10-20 MeV; at 5 MeV, we see a deviation from the pattern established at the higher energies. The spot gets smaller in the x-direction and in the thinner samples in the y-direction. In 10-mm BGO at 5 MeV, but spot size drastically increases as the charge decreases and seems to match the behavior ato 10 MeV for the same thickness. This could indicate spreading in the beam or is just a symptom of the illuminated white reflector artificially increasing the spot size. The RMS spot size calculations give strong weight to high intensity pixels on the edges of the distribution, i.e. far from the centroid.
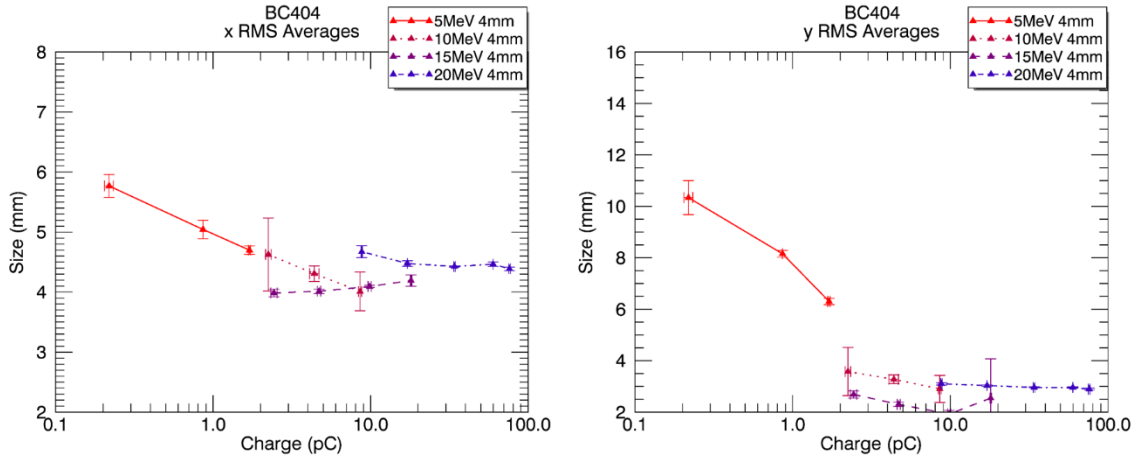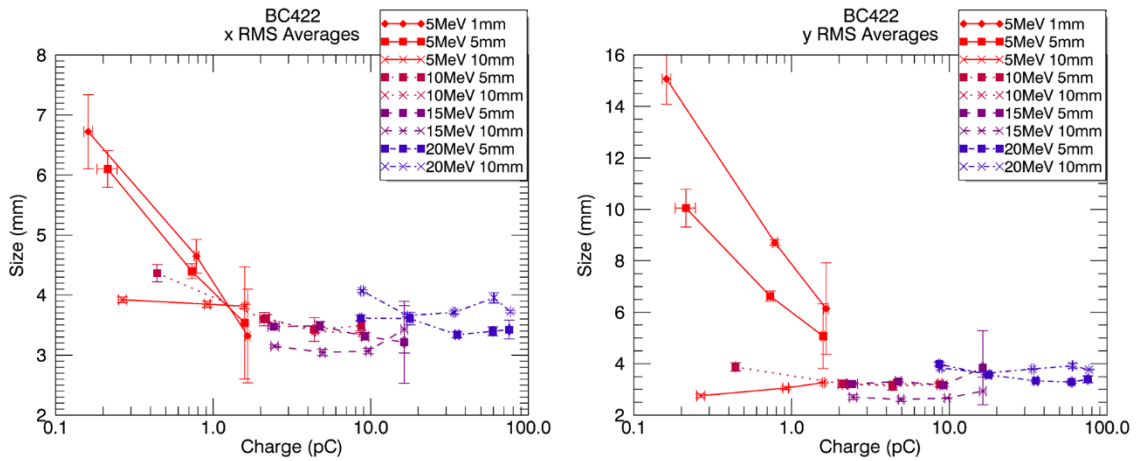
FIG. 30 BC404 RMS spot sizes

FIG. 31 BC422 RMS spot sizes

The Bicron results are shown in FIG. 30 and FIG. 31; note that BC404 is a bulk scintillator and not a pixelated array like the rest of the samples.. In contrast to the non-plastic scintillators, the Bicron samples have smaller spot sizes at higher energies (comparing 10 and 15 MeV) for a given charge. Even with the lack of pixels and make-shift retroreflector of PTFE tape on the front side, the BC404 produces very similar spot sizes to the rest of the samples. The Bicron scintillators also show the highest change in spot size at 5 MeV with varying charge, where major scattering of the electrons/photons in the scintillator blow up the spot. Though, this effect only occurs in the thinner BC422 samples. The scattering occurs in a very thin layer in the scintillator

Some conclusions on the spot size results.

1) In general, each sample produces the same spot size at a given energy and charge. Differences arise when we look into the behavior of a sample over the entire range of beam energies and charges.

2) Lack of spot size variations between bulk BC404 and the pixelated arrays shows that the pixels do not reduce the spot size. We are instead limited by the spread in the electron beam itself,

not the scattering of photons within the scintillator samples. The pixels are too large to have a significant effect on spatial resolution.

3) BC 422 is not a good choice for low energy electrons if you need spatial resolution, which the Compton does. Going with a thicker sample could mitigate these effects.

4) We do see spot size variations as the beam energy changes. However, this could be due to background radiation and scintillation. At the higher energies, we saw an increase in the background light. Backgrounds were taken into account in the calculations; however, if it was not completely eliminated, it would artificially increase the spot size.

3.4.Image Plate Electron Response and Spot Size

Data were taken using GE carestream image plates (IP) to compare to the scintillators. The response of the image plate (per an MCNP model from Rachel Morneau) should be linear in the regime we are looking at (FIG. 32). The data were taken at a fixed energy by putting the IP in the desired location, pulsing the machine, moving the IP a few cm to expose a fresh location, and repeating with a different current to study response vs. charge. The same holder supported both the scintillators and IPs. Each spot represents two shots of the machine because the single shot mode needed to trigger the camera produces two beam pulses. This process was repeated at the energies of 5, 10, 15, and 20 MeV. An example IP is shown in FIG. 33 for the data collected at 10 MeV. This is assuming a reading setting of 100 microns per pixel. The spot looks round and about 6mm in diameter on the image plate.
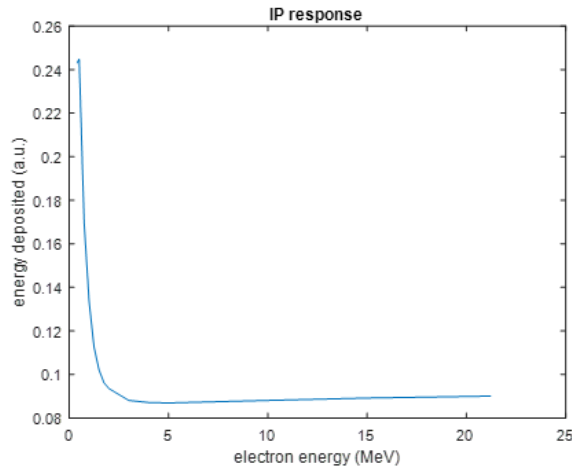

FIG. 32 Electron energy deposition in GE carestream image plates as a function of incident electron energy.
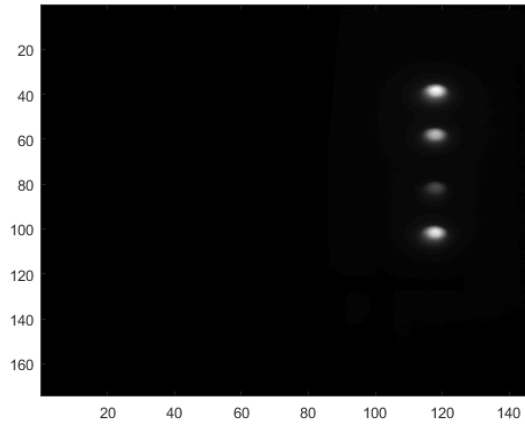
FIG. 33 Scanned image plate data.

The next step in data processing was to crop the data into a region of interest and integrate the charge under each peak. The integration was done by projecting the data along the y axis. A background region (near the beam spot but not on it) was also selected to get an idea of the shape of the background due to scatter. An example of the resulting data is shown. The yellow line is the lineout of the beam spots, the red trace is the background, and the blue trace is the difference.
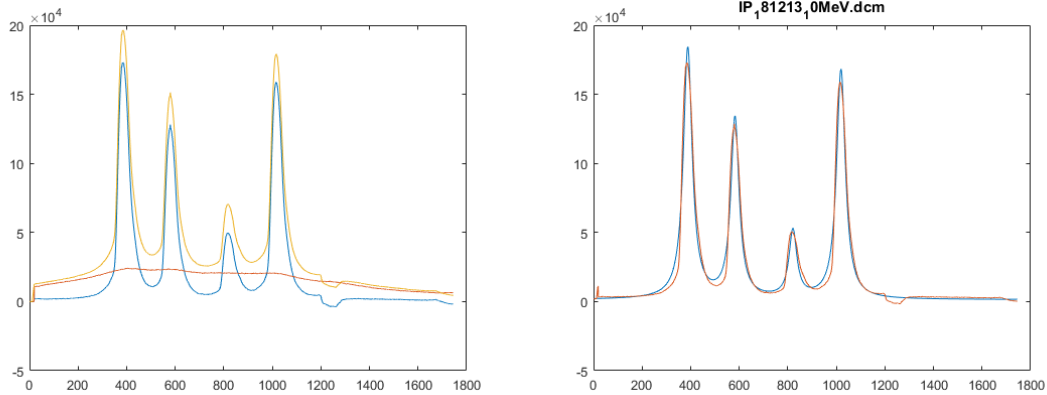

FIG. 34 (Left) Integrated lineouts (projected along the y-axis) of the data in FIG. 33. The yellow trace is the lineout, the orange trace is the background signal, and the blue trace represents their difference. (Right) The corrected lineout data (blue trace) and its Lorentzian fit (orange trace).

The maxima of the peaks was then found and the peaks themselves fit to a Lorentzian. An example of the data vs this fit is shown. The fit is only used to find the centroid and the full-width-at-half-maximum (FWHM) of the peaks. The data is then plotted as either reported current vs. amplitude or reported current vs. the counts under the peak for +/- 2 FWHM. This same procedure was used for all the energies studied. The results are shown below. The data trend is in good agreement with linear for all energies, although the slopes between energies are different. There does not appear to be an appreciable difference between either technique (maximum vs. integrated under peak). We then converted the reported current to charge using the conversion provided by Dave Moir. Plots of counts vs. charge are then shown. As can be seen, the trend is linear and independent of energy. This is consistent with our expectation that the response of the image plate is flat in energy in this regime.
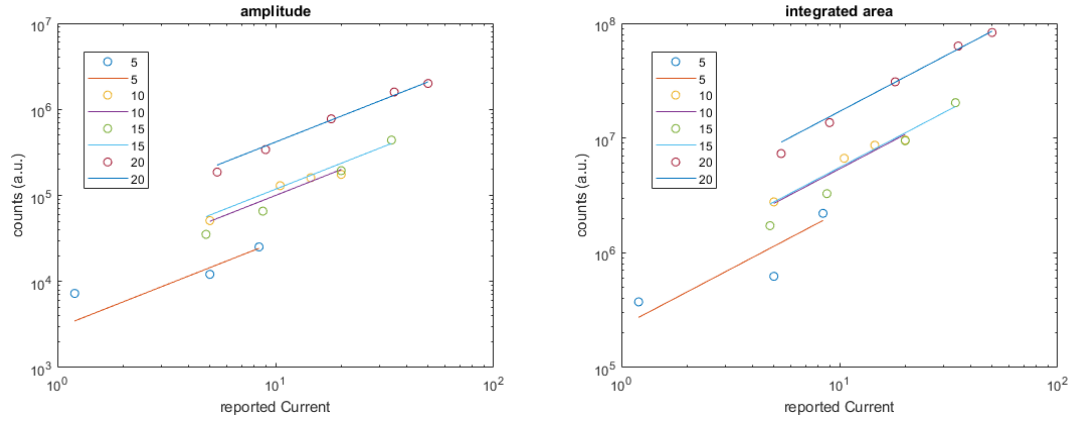
FIG. 35 Integrated area and maximum amplitude of the spots based on the Lorentzian fit to the spots. This is plotted for each beam energy as a function of beam current from the NIBM.
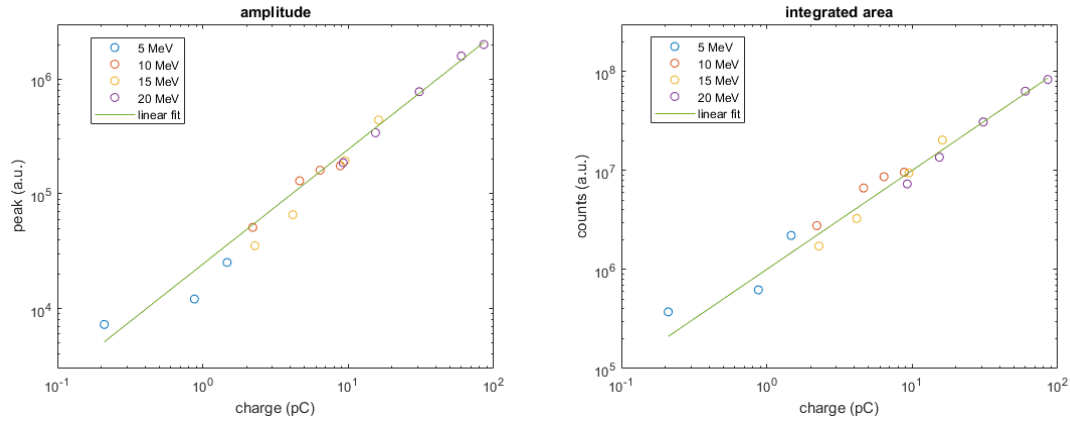

FIG. 36 Same data as FIG. 35, but plotted as a function of total beam charge.

4. Conclusion

We tested the light emission of several commercial scintillator arrays as a function of deposited electron charge and energy at the Idaho Accelerator Center. A charge collector was designed and used to calibrate the electron beam data. Analysis of the scintillator emission spectra and transmission of optical elements allowed for the deconvolution of scintillator intensity and experimental variations into the absolute light output of the arrays. The absolute intensity of emitted light is roughly linear in log-log space with respect to deposited charge, except for the lowest charge at each energy. This implies that the beam energy is fully deposited in the scintillators and the brightness is only dependent on the total number of electrons.

The power law fit of each sample provided a metric for 'good' and 'bad' fits with exponents of B=0.8-1.2 being acceptable, roughly corresponding with a linear trend (B=1). 1) The 5 mm BC-422 and BC-404 samples have the poorest fit. The BC-422 sample may be marginal if we account for the first-point

error and some variation in the 20 MeV data. The BC-404 data is poor and inconclusive. The 20 MeV data is of lesser quality than the other three beam energy data sets. There is greater variation among the sample intensities at that energy and in the reported beam current used to calculate the pulse charge. This agrees with our experience during the 20 MeV run: the machine was operating with less stability. Image plate response to electrons has already been shown to be flat with respect to deposited charge in this energy region. We used this to verify the calibration of the charge collector; the image plates scaled linearly with charge as expected.

The purpose of testing arrays of scintillators rather than bulk samples was to determine if they had any effect on light output or spot size reduction. In general, each sample produced the same spot size at a given energy and charge. Small variations did arise when we look into the behavior of a sample over the entire range of beam energies and charges; spot sizes tended to increase at lower charges and energies. Lack of spot size variations between bulk BC404 and the pixelated arrays shows that the pixels do not reduce the spot size. We are instead limited by the spread in the electron beam itself, not the scattering of photons within the scintillator samples. The pixels are too large to have a significant effect on spatial resolution. BC 422 is not a good choice for low energy electrons if you need spatial resolution, which the Compton does. Going with a thicker sample could mitigate these effects. 1) We do see spot size variations as the beam energy changes. However, this could be due to background radiation and scintillation. At the higher energies, we saw an increase in the background light. Backgrounds were taken into account in the calculations; however, if it was not completely eliminated, it would artificially increase the spot size.

In conclusion, there does not appear to be a clear 'winner' for future Compton spectrometer improvements. BC-422 is clearly the worst choice. If we were to choose a plastic scintillator, it would be best to make it thick and avoid some of the spreading issues. However, this would introduce errors in the imaging plane location of the spectrometer; thinner is better for energy resolution. LYSO has some of the more consistent spot sizes and absolute intensity and is therefore our choice.

Future work will include a more direct comparison of bulk vs segmented output intensity and spot size with LYSO. We also intend to field the Compton spectrometer and the selected samples at both the LANL Microtron and the IAC. These experiments will be targeted to fit the needs of the spectrometer and will compare the scintillators' response to electrons and X rays in the same conditions. In these experiments, we worked with non-ideal conditions. One section of the experimental chamber was not delivered in time and the main camera intended for scintillator imaging stopped communicating with the computer. Vacuum was approximately 2 Torr. The next set of experiments will use the full setup with proper vacuum and optical alignment. The better camera will be used in the next run and a new target holder will be designed to limit changes between samples from breaking vacuum and reseating the scintillators.

Additional improvements are also required of the charge collector. Prior to the IAC experiments, the charge collector mount broke and also damaged its resistors. This, in addition to rotating the assembly to fit through an opening, introduced a lot of variation in charge collector signal quality and magnitude. A new design is currently being planned with the intention of measuring charge before and after each set of current/energy series. The stability of the experimental setup at the IAC will also be improved. Simple shims stopped the pneumatic table from moving during the course of the day, but breaking vacuum and other routine tasks still caused a shift of the entire setup. This cause misalignment on one day and could cause major changes to the amount of deposited charge. We will bring feet next time to ensure the conditions do not change throughout the experiments.